Journal Pre-proof

Small-scale mechanical properties of constitutive phases within a polycrystalline cubic boron nitride composite

H. Besharatloo, S. Gordon, T. Rodriguez-Suarez, A. Can, W.C. Oliver, L. Llanes, J.J. Roa

PII: S0955-2219(19)30581-3

DOI: https://doi.org/10.1016/j.jeurceramsoc.2019.08.023

Reference: JECS 12691

To appear in: *Journal of the European Ceramic Society*

Received Date: 27 May 2019

Revised Date: 26 July 2019

Accepted Date: 17 August 2019

Please cite this article as: Besharatloo H, Gordon S, Rodriguez-Suarez T, Can A, Oliver WC, Llanes L, Roa JJ, Small-scale mechanical properties of constitutive phases within a polycrystalline cubic boron nitride composite, *Journal of the European Ceramic Society* (2019), doi: https://doi.org/10.1016/j.jeurceramsoc.2019.08.023

Small-scale mechanical properties of constitutive phases within a polycrystalline cubic boron nitride composite

H. Besharatloo[1,2], S. Gordon[1,2], T. Rodriguez-Suarez[3], A. Can[3], W. C. Oliver[4], L. Llanes[1,2,*], J. J. Roa[1,2]

[1] CIEFMA - Department of Materials Science and Metallurgical Engineering, EEBE, Technical University of Catalonia-BarcelonaTech, 08019 Barcelona, Spain

[2] Barcelona Research Center in Multiscale Science and Engineering, Technical University of Catalonia-BarcelonaTech, 08019 Barcelona, Spain

[3] Element Six, Global Innovation Centre, Harwell Campus, Didcot OX11 0QR, UK

[4] Nanomechanics, Inc., Oak Ridge, TN 37830, USA

[*]Corresponding author, e-mail: luis.miguel.llanes@upc.edu

Abstract

Micromechanical properties of a polycrystalline cubic boron nitride (PcBN) composite have been assessed by statistical analysis of data gathered from experimental massive nanoindentation. The mechanical study was complemented with electron probe X-Ray microanalysis, aiming to correlate relative B/N ratio and local hardness for individual cBN particles. Best-fit of experimental and deconvoluted data is achieved by considering five mechanically different phases, defined on the basis of chemical nature, TiN/cBN interface presence, ratio between residual imprint dimension and microstructural length scale as well as phase stoichiometry. In-depth local micromechanical and chemical analysis permitted to propose and validate, for the first time, the existence of a correlation between intrinsic hardness and phase stoichiometry for cBN phase. Finally, based on experimental data measured by nanoindentation and analyzed in terms of plastic index, toughness for the PcBN composite studied is estimated to range between 4 and 6 MPa·√m.

Keywords: TiN-cBN; Super-hard multiphase material; Nanoindentation; Statistical method; Small-scale properties.

1. Introduction

Polycrystalline cubic boron nitride (PcBN) is a super-hard multiphase material extensively used in highly demanding applications, such as tooling for high precision abrasive machining processes of alloys employed in the automotive and aerospace industries [1, 2]. The success of PcBN mainly resides in its composite nature, consisting of hard micrometer-sized of cubic boron nitride (cBN) particles bound by a matrix of metal-carbides, nitrides and/or oxides (e.g. Ref. [3, 4]. On one hand, the intrinsic properties of cBN grains are solid attributes, as these provide PcBN with excellent hardness and wear resistance, high temperature stability as well as chemical inertness with respect to ferrous alloys and many other materials. On the other hand, the composite character allows assembling different microstructures by varying size and distribution of hard particles, together with chemical nature and content of the binder. It yields then a wide range of property combinations to satisfy distinct service-related requirements.

Literature information on PcBN cutting tools mainly focuses on machining performance and tool wear, as a function of work piece and/or cutting conditions (e.g. Refs. [5-15]). In general, in these studies, microstructures and properties of studied PcBN tools are rarely invoked as an experimental variable. Furthermore, research addressing the influence of microstructural parameters on basic mechanical or tribological properties of PcBN composite is also quite scarce [16-24]. Considering that an in-depth understanding of microstructure-property relationship has been a key parameter for enhancing functionality of other multiphase hard materials (e.g. cemented carbides [25-27] among others), the lack of this information clearly points out the need for research efforts in this

direction for super hard ceramic composites, and in particular for PcBN composites. Following the above ideas, this work aims to assess, document and analyze the small-scale mechanical properties (i.e. at the length scale of constitutive phases) of a PcBN composite. It is done by implementing systematic micromechanical testing protocols: experimental massive nanoindentation and statistical analysis of the gathered data, complemented with advanced characterization techniques of its microstructure. Such approach is expected to provide relevant knowledge towards microstructural design optimization of PcBN composites.

2. Experimental procedure

2.1. Material and microstructural characterization

A commercial ceramic/ceramic composite grade, cBN-TiN, was investigated. It was supplied as an insert brazed to a hardmetal (WC-Co) substrate. Prior to detailed microstructural and small-scale mechanical characterization, the specimen was chemo-mechanically polished by using diamond suspensions with gradually decreasing particle sizes, from 30 down to 1 μm. Afterwards, the sample was carefully polished with OPAN for 40 min; and thus, ultrasonically cleaned with acetone during 15 min and dried using pure air.

Field Emission Scanning Electron Microscopy (FESEM, JEOL 7100F) was used to inspect the ceramic/ceramic microstructure. It was done by analyzing multiple micrographs in terms of phase content and cBN particle size. Volume fractions of cBN particles and ceramic binder were calculated from two-dimension data, attained by direct image correlation using the ImageJ software. Meanwhile, mean particle size of cBN grains was determined by means of the conventional linear intercept method [28]. This quantitative microstructural analysis was complemented by energy dispersive X-ray spectroscopy (EDS), in order to evaluate chemical nature of each constitutive phase.

Aiming for detailed characterization of nitrogen content within cBN particles, electron probe X-ray microanalysis (EPMA) was conducted. It was done by using a JEOL JXA-8230 microprobe and wavelength dispersive spectrometer (WDS) attached to this equipment. X-ray map for the nitrogen was recorded in high-resolution mode, using a channel width of 1 eV. Electron currents were selected to ensure that counting rates were less than 10^4 counts·sec^{-1}. More information about the protocol followed to conduct this analysis may be found in Refs. [29, 30]. Two different nitrogen maps in the cBN-TiN specimen were attained, with counting times that ensured a statistical uncertainty lower than 1 %.

2.2. Micromechanical properties: indentation testing

2.2.1. Hardness: Massive indentation and statistical analysis

Nanoindentation measurements were performed using two distinct nanoindentation units as well as following different protocols regarding testing conditions. First, reference values for hardness of each constitutive phase were assessed by carrying out three 10 x 10 indentation matrices working under displacement control mode. It was done by imposing a maximum displacement into surface of 200 nm and a distance between imprints of 5 μm. Matrices were conducted in at least three different (randomly selected) locations at the surface of the PcBN composite studied, yielding similar results in all the cases. These tests were conducted with a Nanoindenter XP (MTS) equipped with a continuous stiffness measurement (CSM) modulus and a Berkovich diamond tip. Calibration of the contact area of the tip was done with fused silica – known value of Young's

modulus of 72 GPa and Poisson's ratio of 0.17 [31]. As a result of these tests, it was found that maximum values of applied load (corresponding to 200 nm indentation depth) were in the range of 25-30 mN. In order to document subsurface deformation and damage scenario associated with Berkovich nanoindentations confined within individual phases, cross-sections were prepared by means of Focused Ion Beam (FIB) coupled to a Zeiss Neon 40 FESEM. Prior to FIB milling, a protective thin platinum layer was deposited on the residual imprints to be studied. A Ga^+ source was used, and current as well as acceleration voltage were continuously decreased down to a final polishing stage at 500 pA at 30 kV.

Following the above study, two additional nanoindentation testing protocols were performed by implementation of novel high-speed and micromechanical mapping experimental upgrades. They were conducted under loading control using an iMicro® Nanoindenter (Nanomechanics Inc.). Load and depth data attained in all the above nanoindentation tests were analyzed by using the standard method proposed by Oliver and Pharr, which leads to determine contact stiffness and hardness [31, 32]. Different maximum applied loads and grid sizes were used, aiming to optimize data acquisition towards reliable determination of hardness values, within the framework of the statistical method proposed by Ulm and coworkers [33-36]. On one hand, 2500 (50 x 50 grid) imprints at maximum applied load of 25 mN were done in an area of 50 x 50 μm^2. On the other hand, 12500 imprints at maximum applied load of 10 mN were performed. The latter were divided into 2 matrices of 100 x 100 and 50 x 50 indentations in areas of 50 x 50 μm^2 and 25 x 25 μm^2, respectively. The indentation spacing was chosen as per the recommendation of Phani and Oliver [37]. For these tests, Nanoblitz software was used to attain a mechanical property mapping at high speed, each test being performed in less than 1 second. The fast testing capability enables mapping

over large areas in a short amount of time as well as access to large data sets for statistical analysis. In all the cases, a sharp Berkovich tip (calibrated as indicated above) was used. Contact stiffness was continuously measured as a function of depth using a phase lock amplifier oscillating at 100 Hz frequency and 2 nm displacement amplitude.

Obtained hardness results were then statistically analyzed, according to the method proposed by Ulm and coworkers [33-36]. Such testing and data analysis protocol has been recently validated for other hard and microstructurally heterogeneous materials, such as WC- and Ti(C,N)- based cemented carbides, by the authors of this study [38-41]. Theoretical framework behind this approach is based on: (1) consideration of the heterogeneous system as composed by several distinct phases with different mechanical properties *(H)*; (2) assumption of mechanical properties of each phase to follow Gaussian distributions (p_i), as given by:

$$p_i = \frac{1}{\sqrt{2\pi\sigma_i^2}} e^{\left(-\frac{[H-H_i]^2}{2\sigma_i^2}\right)} \quad (1)$$

where H_i is the arithmetic mean for each indentation (N_i) on each constitutive phase *(i)* and σ_i is the standard deviation; (3) generation of experimental cumulative distribution function (CDF) for each constitutive (Gaussian distributed) phase, written as follows:

(2)

$$CDF = \sum_{i}^{n} \frac{1}{2} f_i \operatorname{erf}\left[\frac{H - H_i}{\sqrt{2}\sigma_i}\right]$$

where f_i is the volume fraction of a mechanically identifiable phase [33]; and (4) final deconvolution of experimental CDFs, yielding then mean and standard deviation of *H* for each mechanical phase. In this investigation, considering the ratio between residual imprint dimensions and microstructural length scales, three mechanically different phases were originally defined. Two of them correspond to the two microstructurally distinct constitutive phases, i.e. cBN particles and TiN matrix. The third one refers to a "composite-like" phase, and is related to events where imprints were indeed probing combined mechanical response of both constituents, i.e. cBN and TiN. Details of the statistical method followed may be found elsewhere [38].

Finally, aiming to evaluate relative *H* of cBN particles regarding nitrogen or boron amount diffused in the grains, an additional study was conducted in all three 10 x 10 indentation matrices performed following the first testing protocol described above. There, a correlation between intrinsic *H* and local chemical composition was attempted by comparison of micromechanical mapping data with results attained from EPMA analysis within a defined region, limited for easier identification by a FIB-marked square (see **Figure 5a**).

2.2.2. Indentation fracture toughness: cube corner indentation

Indentation fracture toughness (K_{Ic}) in ceramic materials is commonly measured by means of indentation techniques, as follows [42, 43]:

$$K_{Ic} = \alpha \left(\frac{E}{H}\right)^{1/2} \left(\frac{P}{C^{3/2}}\right) \quad (3)$$

where H is the hardness, E is the elastic modulus (assessed from nanoindentation tests described in previous section), P is the maximum indentation load, c is the radial crack length created in the residual imprint, and α is an empirical constant related to the indenter geometry.

In order to estimate K_{Ic} of the entire PcBN composite, six different loads (i.e. 5, 10, 20, 30, 40 and 50 gf) and five indentations per load were done, under load control mode and using a cube-corner indenter. This indenter was used, instead of a Berkovich one, because the higher sharpness of the former; hence, plasticity is induced earlier. Load (P) – displacement (h) data was also recorded in these tests. Corresponding P – h curves showed several pop-ins, i.e. plateaus at given load levels observed during loading part. This phenomenon is related with the onset of plasticity on the material. Within this context, pop-ins could be associated with nucleation of dislocations, crack formation, rupture and/or phase transformation. Data recording was complemented with high-resolution images of the residual imprints as well as transversal sections of them, obtained by

means of FESEM/FIB. It was done to analyze the damage induced in the material and try to correlate it with microstructure and mechanical response.

3. Results and discussions

3.1. Microstructural characterization

The volume fraction (vol. %) of cBN particles is estimated to be 70%. Meanwhile, mean particle size of cBN grains and binder mean free path (λ) are discerned to be about 2.7 and 2.0 μm respectively. The main microstructural parameters are summarized in **Table 2**. These microstructural findings were complemented by an EDS analysis, which indicated presence of aluminum, besides other expected elements (**Table 1**). Addition of aluminum is a common practice during PcBN manufacturing for enhancing adhesion and wettability between cBN particles and TiN binder, as reported in Ref. [44].

3.2. Small-scale hardness

3.2.1. Reference hardness values of the constitutive phases

Figure 1a shows a FESEM micrograph corresponding to a small array of indentations (performed at 200 nm of maximum penetration depth). From such image, it is evident that some residual imprints are completely allocated within one of the two constitutive phases. This is the case for imprints encircled with blue and yellow dashed lines for TiN and cBN particles, respectively. On the other hand, it is also clear that there are many other indentations which are indeed assessing

the mechanical response of the composite itself, as residual imprints are probing regions including phase boundaries. In those cases, corresponding plastic flow would be expected to interact with both phases (imprints encircled with red dashed lines in **Figure 1a**). Such a scenario, directly related to the ratio between residual imprint dimension and microstructural length scale for the material studied, supports the above definition of three mechanically different phases for the PcBN system under consideration: two microstructurally distinct constitutive phases, i.e. cBN particles and TiN matrix, and a third phase corresponding to one exhibiting the "composite-like" response.

Figure 2 shows *H* evolution as a function of penetration depth until reaching 200 nm, for each mechanically different phase. All the curves tend to get into plateau values for penetration depths higher than 100 nm. Under these conditions, reference values for the intrinsic *H* of each constitutive phase, i.e. independent of size or scale effects, may be estimated to be around 20 and 42 GPa for TiN binder and cBN particles, respectively. On the other hand, intermediate *H* values, in a range defined by those assessed for individual phases, could be expected for the third composite phase. These values are in satisfactory agreement with those reported by different research groups for bulk TiN (see references [45-48]) and PcBN composites (see references [17-19, 23, 24]).

In order to implement statistical method to obtain small-scale properties of each mechanical phase under consideration, plastic flow (affecting a region with dimensions about 10 times maximum penetration depth [37]) must be confined inside each phase. **Figures 1c** and **1e** shows FIB-milled cross-section images of subsurface scenario for individual imprints, pointed by arrows in **Figure**

1a and detailed in **Figures 1b** and **1d**. It is clear in both cases that above condition (plastic flow region, defined by white dashed line, completely embedded within the individual phase) is satisfied for imprints performed within binder and particles. This validates the consideration of each nanoindentation test as an individual event regarding subsequent statistical analysis of the gathered data.

3.2.2. Massive nanoindentation and statistical analysis

Hardness histograms (with a constant bin size of 1 GPa) corresponding to experimental data attained out of the 15000 indentations performed following the high-speed testing protocols are shown in **Figure 3**. They are determined from data with different numbers of imprints and maximum applied load: 12500 indentations at 10 mN (**Figure 3a**) and 2500 imprints at 25 mN (**Figure 3b**). By applying the statistical method proposed by Ulm and co-workers [33-36], it is possible to further deconvolute the experimental data into three peaks with different mean values, as summarized in **Table 3**. Following the reference values assessed before, the higher and lower peaks can be attributed to cBN particles and TiN binder, whereas the intermediate one must be related to the composite-like phase defined by phase boundary regions. Statistical analysis of the data gathered using distinct maximum applied load levels do not yield relevant differences in mean and standard deviation of small-scale *H* values. However, data attained imposing a load of 25 mN (as compared to 10 mN) do yield a better screening among Gaussian distributions for each defined phase. Main reason behind it may be related to size-scale effects (e.g. surface roughness) or influence of indenter tip defects, these being more critical for shallower penetrations.

Very interesting, from direct observation of the obtained histograms (gray filled areas "marked by arrows" around the red Gaussian distribution curves in **Figure 3**), it could be speculated that analysis of cBN data would be better-fitted by considering two additional populations, corresponding to harder and softer (with respect to the original main peak) cBN particles. These differences could be related to variations of chemical composition within cBN particles, and this aspect will be addressed later in this study.

3.2.3. Hardness cartography map

One of the advantages of implementing novel high-speed nanoindentation testing protocols is that they are inherently associated with gathering of large amounts of data, small penetration depths and close spacing of indents. This altogether allows enhancing accuracy and statistical significance of data attained, including assessment of values corresponding to smaller length scale regions than individual phases themselves.

Figure 4 presents *H* cartography maps for the PcBN composite studied. As before, they correspond to testing done using two different levels of maximum applied load. Maps have been obtained from bicubic interpolation using 12500 and 2500 indents performed at 10 and 25 mN of maximum applied load respectively (**Figure 4a** and **Figure 4b,** respectively). As already commented from results presented in **Figure 3** and **Table 3**, *H* for the TiN phase is observed to range between 15

and 25 GPa, in fair agreement with the data reported in the literature (e.g. Ref.[49]). On the other hand, cBN particles show not only higher *H* values, but also a much wider scatter, i.e. between 45 and 80 GPa. Finally, intermediate *H* values are discerned for regions containing phase boundaries, i.e. composite-like nature, where binder and particles are somehow interdispersed or clearly interacting with each other. Regarding property resolution, it is interesting to highlight the higher level attained when imposing lower applied loads (i.e. 10 mN as compared to 25 mN). This must be associated with the lower effective ratio existing between imprint size and microstructural length scale as applied load decreases. However, care should be taken here on the final data analysis, as size (either surface or just length-related) effects may not be neglected as penetration depth becomes extremely shallow.

3.2.4. Chemical nature effects on the small-scale hardness of cBN particle

As it was commented in **Section 3.2.2**, deeper analysis of the histograms shown in **Figure 3** points out that better-fitting of the experimental data could be attained by considering three different small-scale *H* peaks (instead of just one) for cBN particles as related to chemical nature effects. This hypothesis was proposed on the basis of findings reported by Sachdev [50] who states that morphology and residual stresses of cBN crystals may be directly related to impurity effects as well as different N and B contents along the particle. In this regard, B rich (which implies particles deficient of N) cBN is prone to form B clusters in some specific crystalline planes, finally yielding octahedral/irregular shaped grains with their crystallographic packaging distorted. Within this context, the two extra peaks referred above (see grey arrows in **Figure 3**) could then be rationalized

on the basis of possible non-stoichiometry effects on measured *H* of cBN particles, as far as these differences could be discriminated by the massive indentation and statistical analysis protocol implemented in this study.

Attempting to shed some light on this matter, EMPA analysis was used to establish the composition of small areas of the material studied where a homogeneous indentation array was subsequently performed, under displacement control mode at 200 nm of maximum penetration depth into surface. Main goal behind it was to evaluate possible correlation between N amount and small-scale *H* of individual cBN particles (where indentations were absolutely confined within the cBN phase, see black circles in **Figure 5b**).

From the images shown in **Figure 6a**, following EPMA analysis, cBN particles could be classified in three different groups, depending upon relative B/N content in atomic % (at. %): stoichiometric (50/50), and non-stoichiometric - either B-poor (B at. % content lower than 25 **Figure 6b**) or B-rich (B at. % content higher than 75 **Figure 6c**). Although specific reasons for non-stoichiometry of cBN particles is out of the scope of this investigation, it could be speculated to result, following recent findings by Dios *et al.* [51], from element diffusion between TiN binder and cBN particles during the sintering stage. Taking this into consideration, small-scale *H* data may then be assessed for cBN particles as a function of relative B/N content. **Figure 7a** shows representative mechanical response, in terms of *H* against the displacement into surface, exhibited by three cBN particles with different chemical composition. From these results, it is discerned that B-poor particles are clearly harder than B-rich ones, yielding support to the consideration of three mechanically

different cBN phases for reliable assessment of small-scale mechanical properties of the PcBN here studied (**Figure 7b** and **Table 4** with fitted small-scale *H* for 5 mechanically different phases).

3.3. Indentation fracture toughness

Figure 8 shows a representative *P – h* curve recorded when indenting, up to 50 gf, for the material studied. Different pop-ins are discerned in the loading curve, possibly in direct relation to irreversible deformation and damage phenomena induced on the material. **Figure 9** shows residual imprints resulting after cube-corner indentations conducted at different applied loads (from 5 to 50 gf). Independent of applied load, radial cracks emanating at the corners of the residual imprints are always absent. At applied load level of 10gf, material pile-up comes out around the residual imprints (**Figure 9a** and **Figure 9b**). It is intensified as maximum applied load increases. As applied load gets higher than 20gf, cracking and chipping are identified as additional damage-induced events (**Figure 9c**, **Figure 9d**, **Figure 9e** and **Figure 9f**).

FESEM/FIB inspection on transversal sections of residual imprint performed at 50 gf of maximum applied load (**Figure 10a**) allows inspection of damage scenario and crack-microstructure interaction induced by the cube corner indentation. Very interesting, it is discerned that besides lateral cracking (white arrow in **Figure 10b**), crack bridging (white dashed circle shown in **Figure 10c**) also develops. In this regard, it is found that the former nucleates at the material subsurface and runs parallel to the surface. However, as applied stress rises, the lateral cracks emerges into the surface and induces chipping. During this damage evolution, crack propagation seems to take

place mostly through the ceramic binder or ceramic/ceramic interfaces, exhibiting local deflections as it meets the harder cBN particles.

Taking into account that well-developed radial cracks are not observed in the residual imprints (**Figure 9**), conventional indentation micro-fracture method (i.e. through **equation 3**) cannot be implemented for quantitative assessment of indentation fracture toughness. However, as illustrated in this equation, this parameter mainly depends on the ratio between *H* and elastic modulus (*E*) of the material. Within this context, a qualitatively estimation of the effective toughness of the composite studied may be done by invoking the plasticity index ($PI = H/E$ [52, 53]). In general, lower plasticity index values are linked to higher effective toughness levels. From gathered data of nanoindentation testing (as referred in previous sections), mean values for macroscopic *E* and *H* for the PcBN composite may be taken as 650 GPa and 35 GPa, respectively. It results in a *PI* value around $5 \cdot 10^{-2}$. For comparison purposes, such value is close to *PI* levels exhibited by other hard ceramic materials such as WC (*E* and intrinsic *H* values in the ranges of 475-650 GPa and 25-33 GPa, respectively [38, 39]). Hence, effective toughness for the PcBN composite system studied here may be estimated to range between 4 and 6 MPa·√m [54, 55], in agreement with lower-bound results reported in the literature for those composites [17, 23, 24].

4. Conclusions

A systematic investigation, aiming to assess micromechanical properties of the constitutive phases of a PcBN composite has been conducted. The mechanical study has been complemented by the use of advanced characterization techniques such as FESEM/FIB and EPMA. Based on the obtained data the following conclusions may be drawn:

- A protocol based on massive nanoindentation and statistical analysis was successfully implemented for assessing small-scale mechanical properties of a PcBN composite. In doing so, the heterogeneous system was originally considered as constituted by three distinct phases with different mechanical properties: two of them microstructurally different, i.e. cBN particles and TiN matrix, and a third phase corresponding to one exhibiting the "composite-like" response. Within this context, intrinsic *H* values of about 20 and 50 GPa were assessed for TiN binder and cBN grains as lower and upper bounds to the hardness range determined for the composite-like phase, i.e. between 30 and 40 GPa.

- Mean and standard deviation of small-scale *H* values are independent, within the experimental set outs used in this study, of maximum applied load and number of experimental events (indentations) accounted. However, data attained imposing different load levels, i.e. 25 mN or 10 mN, yielded either better screening among Gaussian distributions for each defined phase or higher microstructure-property resolution within hardness mapping, respectively. Such differences are related to distinct relevance of size-

scale effects (e.g. surface roughness) or indenter tip defects depending upon penetration depth.

- An in-depth statistical analysis of the upper-level *H* data complemented with implementation of advanced characterization techniques (i.e. combined EMPA, instrumented nanoindentation and FESEM) pointed out and validated the consideration of additional mechanically different cBN-related phases on the basis of relative B/N content. To the best knowledge of the authors, it is the first time that different intrinsic *H* values are reported for cBN particles as a function of phase (B/N ratio) stoichiometry.

- Direct quantitative measurement of K_{Ic} for the composite was not possible because absence of radial cracks emanating from corners of residual imprints. However, *PI* assessment and subsequent comparison with literature data for WC ceramics, points out that toughness for TiN-cBN composite investigated ranges between 4 and 6 MPa·$m^{1/2}$.

Acknowledgments

The current study was supported by the Spanish Ministerios de Economía y Competitividad MINECO y de Ciencia, Innovación y Universidades MICINN - FEDER through grants MAT2015-70780-C4-3-P and PGC2018-096855-B-C41 respectively, and by the industry-university collaborative program between Element Six and UPC. J.J.Roa acknowledges the Serra Hunter program of the Generalitat de Catalunya.

References

[1] M. Cook, P. Bossom, Trends and recent developments in the material manufacture and cutting tool application of polycrystalline diamond and polycrystalline cubic boron nitride, Int. J. Refract. Met. Hard. Mater. 18 (2000) 147-152. https://doi.org/10.1016/S0263-4368(00)00015-9.

[2] R. M'Saoubi, D. Axinte, S.L. Soo, C. Nobel, H. Attia, G. Kappmeyer, S. Engin, W.-M. Sim, High performance cutting of advanced aerospace alloys and composite materials, CIRP Annals. 64 (2015) 557-580. https://doi.org/10.1016/j.cirp.2015.05.002.

[3] J. Angseryd, M. Elfwing, E. Olsson, H.-O. Andrén, Detailed microstructure of a cBN based cutting tool material, Int. J. Refract. Met. Hard. Mater. 27 (2009) 249-255. https://doi.org/10.1016/j.ijrmhm.2008.09.008.

[4] S. Fang, L. Llanes, D. Bähre, F. Mücklich, 3D characterization of cubic boron nitride (CBN) composites used as tool material for high precision abrasive machining processes, Ceram. Int. 43 (2017) 14693-14700. https://doi.org/10.1016/j.ceramint.2017.07.198.

[5] J. Arsecularatne, L. Zhang, C. Montross, Wear and tool life of tungsten carbide, PCBN and PCD cutting tools, Int. J. Mach. Tool Manu. 46 (2006) 482-491. https://doi.org/10.1016/j.ijmachtools.2005.07.015.

[6] C. Lahiff, S. Gordon, P. Phelan, PCBN tool wear modes and mechanisms in finish hard turning, Robot. Comput. Integr. Manuf. 23 (2007) 638-644. https://doi.org/10.1016/j.rcim.2007.02.008.

[7] K. Katuku, A. Koursaris, I. Sigalas, Wear mechanisms of PcBN cutting tools when dry turning ASTM Grade 2 austempered ductile iron under finishing conditions, Wear. 268 (2010) 294-301. https://doi.org/10.1016/j.wear.2009.08.027.

[8] M. Okada, A. Hosokawa, R. Tanaka, T. Ueda, Cutting performance of PVD-coated carbide and CBN tools in hardmilling, Int. J. Mach. Tool Manu. 51 (2011) 127-132. https://doi.org/10.1016/j.ijmachtools.2010.10.007.

[9] V. Bushlya, J. Zhou, J.-E. Ståhl, Effect of cutting conditions on machinability of superalloy Inconel 718 during high speed turning with coated and uncoated PCBN tools, Proc. CIRP. 3 (2012) 370-375. https://doi.org/10.1016/j.procir.2012.07.064.

[10] R. M'Saoubi, M.P. Johansson, J.M. Andersson, Wear mechanisms of PVD-coated PCBN cutting tools, Wear. 302 (2013) 1219-1229. https://doi.org/10.1016/j.wear.2013.01.074.

[11] M.A. Shalaby, M.A. El Hakim, M.M. Abdelhameed, J.E. Krzanowski, S.C. Veldhuis, G.K. Dosbaeva, Wear mechanisms of several cutting tool materials in hard turning of high carbon–chromium tool steel, Tribol. Int. 70 (2014) 148-154. https://doi.org/10.1016/j.triboint.2013.10.011.

[12] S. Saketi, S. Sveen, S. Gunnarsson, R. M'Saoubi, M. Olsson, Wear of a high cBN content PCBN cutting tool during hard milling of powder metallurgy cold work tool steels, Wear. 332 (2015) 752-761. https://doi.org/10.1016/j.wear.2015.01.073.

[13] G.K. Dosbaeva, M.A. El Hakim, M.A. Shalaby, J.E. Krzanowski, S.C. Veldhuis, Cutting temperature effect on PCBN and CVD coated carbide tools in hard turning of D2 tool steel, Int. J. Refract. Met. Hard. Mater. 50 (2015) 1-8. https://doi.org/10.1016/j.ijrmhm.2014.11.001.

[14] O. Gutnichenko, V. Bushlya, J. Zhou, J.-E. Ståhl, Tool wear and machining dynamics when turning high chromium white cast iron with pcBN tools, Wear. 390 (2017) 253-269. https://doi.org/10.1016/j.wear.2017.08.005.

[15] L. Chen, J.-E. Stahl, W. Zhao, J. Zhou, Assessment on abrasiveness of high chromium cast iron material on the wear performance of PCBN cutting tools in dry machining, J. Mater. Process. Technol. 255 (2018) 110-120. https://doi.org/10.1016/j.jmatprotec.2017.11.054.

[16] R.M. Erasmus, J.D. Comins, M.L. Fish, Raman and photoluminescence spectra of indented cubic boron nitride and polycrystalline cubic boron nitride, Diam. Relat. Mater. 9 (2000) 600-604. https://doi.org/10.1016/S0925-9635(00)00241-7.

[17] A. McKie, J. Winzer, I. Sigalas, M. Herrmann, L. Weiler, J. Rödel, N. Can, Mechanical properties of cBN–Al composite materials, Ceram. Int. 37 (2011) 1-8. https://doi.org/10.1016/j.ceramint.2010.07.034.

[18] M. A. Umer, P. H. Sub, D. J. Lee, H. J. Ryu, S. H. Hong, Polycrystalline cubic boron nitride sintered compacts prepared from nanocrystalline TiN coated cBN powder, Mater. Sci. Eng. A. 552 (2012) 151-156. https://doi.org/10.1016/j.msea.2012.05.024.

[19] K. Maweja, L. Cornish, N. Can, Polycrystalline cubic boron nitride sintered with Ti (C, N)-W-Al mechanically alloyed binders, J. Eur. Ceram. Soc. 32 (2012) 3593-3601. https://doi.org/10.1016/j.jeurceramsoc.2012.05.011.

[20] D. Carolan, A. Ivanković, N. Murphy, A combined experimental–numerical investigation of fracture of polycrystalline cubic boron nitride, Eng. Fract. Mech. 99 (2013) 101-117. https://doi.org/10.1016/j.engfracmech.2012.09.008.

[21] P. Alveen, D. McNamara, D. Carolan, N. Murphy, A. Ivanković, The influence of microstructure on the fracture properties of polycrystalline cubic boron nitride, Comp. Mater. Sci. 109 (2015) 115-123. https://doi.org/10.1016/j.commatsci.2015.06.036.

[22] Y. Ichida, H. Ohfuji, T. Irifune, Y. Kojima, T. Shinmei, Synthesis of ultrafine nano-polycrystalline cubic boron nitride by direct transformation under ultrahigh pressure, J. Eur. Ceram. Soc. 38 (2018) 2815-2822. https://doi.org/10.1016/j.jeurceramsoc.2018.02.023.

[23] L. Li, Y. Zhao, K. Sun, H. Ji, D. Feng, Z. Li, Composition, microstructure and mechanical properties of cBN-based composites sintered with AlN-Al-Ni binder, Ceram. Int. 44 (2018) 16915-16922. https://doi.org/10.1016/j.ceramint.2018.06.130.

[24] K. Slipchenko, V. Turkevich, I. Petrusha, V. Bushlya, J.-E. Ståhl, Superhard pcBN materials with chromium compounds as a binder, Procedia Manuf. 25 (2018) 322-329. https://doi.org/10.1016/j.promfg.2018.06.090.

[25] H. E. Exner, Physical and chemical nature of cemented carbides, Int. Mater. Rev. 24 (1979) 149-173. https://doi.org/10.1179/imtr.1979.24.1.149.

[26] B. Roebuck, E. Almond, Deformation and fracture processes and the physical metallurgy of WC–Co hardmetals, Int. Mater. Rev. 33 (1988) 90-112. https://doi.org/10.1179/imr.1988.33.1.90.

[27] L. Prakash, Fundamentals and general applications of hardmetals, in: V. K. Sarin, D. Mari, L. Llanes (Eds), Comprehensive hard materials, Elsevier Ltd, Oxford, 2014, pp. 29-90.

[28] Metallographic Determination of Microstructure. Part 2: Measurement of WC GrainSize, in: ISO 4499-2: 2008, Hardmetals, Geneva, 2008.

[29] C. Merlet, X. Llovet, F. Salvat, Measurements of the surface ionization in multilayered specimens, , X-ray spectrum. 33 (2004) 376-386. https://doi.org/10.1002/xrs.757.

[30] C. Merlet, X. Llovet, O. Dugne, S. Brémier, W. Van Renterghem, R. Restani, Virtual standard for wavelength-dispersive electron-probe microanalysis, Microchim. Acta. 161 (2008) 427-432. https://doi.org/10.1007/s00604-007-0856-2.

[31] W. C. Oliver, G. M. Pharr, An improved technique for determining hardness and elastic modulus using load and displacement sensing indentation experiments, J. Mater. Res. 7 (1992) 1564-1583. https://doi.org/10.1557/JMR.1992.1564.

[32] W. C. Oliver, G. M. Pharr, Measurement of hardness and elastic modulus by instrumented indentation: Advances in understanding and refinements to methodology, J. Mater. Res. 19 (2004) 3-20. https://doi.org/10.1557/jmr.2004.19.1.3.

[33] G. Constantinides, F.-J. Ulm, K. Van Vliet, On the use of nanoindentation for cementitious materials, Mater. Struct. 36 (2003) 191-196. https://doi.org/10.1007/BF02479557.

[34] G. Constantinides, K. S. Ravi Chandran, F. J. Ulm, K. J. Van Vliet, Grid indentation analysis of composite microstructure and mechanics: Principles and validation, Mater. Sci. Eng. A. 430 (2006) 189-202. https://doi.org/10.1016/j.msea.2006.05.125.

[35] G. Constantinides F.-J. Ulm, The nanogranular nature of C–S–H, J. Mech. Phys. Solids. 55 (2007) 64-90. https://doi.org/10.1016/j.jmps.2006.06.003.

[36] F.-J. Ulm, M. Vandamme, C. Bobko, J. Alberto Ortega, K. Tai, C. Ortiz, Statistical Indentation Techniques for Hydrated Nanocomposites: Concrete, Bone, and Shale, J. Am. Ceram. Soc. 90 (2007) 2677-2692. https://doi.org/10.1111/j.1551-2916.2007.02012.x.

[37] P. S. Phani, W.C. Oliver, A critical assessment of the effect of indentation spacing on the measurement of hardness and modulus using instrumented indentation testing, Mater. Des. 64 (2019) 107563. https://doi.org/10.1016/j.matdes.2018.107563.

[38] J.J. Roa, E. Jiménez-Piqué, C. Verge, J.M. Tarragó, A. Mateo, J. Fair, L. Llanes, Intrinsic hardness of constitutive phases in WC–Co composites: Nanoindentation testing, statistical analysis, WC crystal orientation effects and flow stress for the constrained metallic binder, J. Eur. Ceram. Soc. 35 (2015) 3419-3425. https://doi.org/10.1016/j.jeurceramsoc.2015.04.021.

[39] J. J. Roa, P. S. Phani, W. C. Oliver, L. Llanes, Mapping of mechanical properties at microstructural length scale in WC-Co cemented carbides: Assessment of hardness and elastic modulus by means of high speed massive nanoindentation and statistical analysis, Int. J. Refract. Met. Hard. Mater. 75 (2018) 211-217. https://doi.org/10.1016/j.ijrmhm.2018.04.019.

[40] D. A. Sandoval, J. J. Roa, O. Ther, E. Tarrés, L. Llanes, Micromechanical properties of WC-(W, Ti, Ta, Nb) C-Co composites, J. Alloys. Compd. 777 (2019) 593-601. https://doi.org/10.1016/j.jallcom.2018.11.001.

[41] H. Besharatloo, M. de Nicolás, J.J. Roa, M. Dios, A. Mateo, B. Ferrari, E.Gordo, L. Llanes, Assessment of mechanical properties at microstructural length scale of Ti(C,N)–FeNi ceramic-metal composites by means of massive nanoindentation and statistical analysis, Ceram. Int. (2019) in press, https://doi.org/10.1016/j.ceramint.2019.06.292.

[42] B. R. Lawn, A. Evans, D. Marshall, Elastic/plastic indentation damage in ceramics: the median/radial crack system, J. Am. Ceram. Soc. 63 (1980) 574-581. https://doi.org/10.1111/j.1151-2916.1980.tb10768.x.

[43] G. Pharr, Measurement of mechanical properties by ultra-low load indentation, Mater. Sci. Eng. A. 253 (1998) 151-159. https://doi.org/10.1016/S0921-5093(98)00724-2.

[44] Y. Yuan, X. Cheng, R. Chang, T. Li, J. Zang, Y. Wang, Y. Yu, J. Lu, X. Xu, Reactive sintering cBN-Ti-Al composites by spark plasma sintering, Diam. Relat. Mater. 69 (2016) 138-143. https://doi.org/10.1016/j.diamond.2016.08.009.

[45] H. Kuwahara, N. Mazaki, M. Takahashi, T. Watanabe, X. Yang, T. Aizawa, Mechanical properties of bulk sintered titanium nitride ceramics, Mater. Sci. Eng. A. 319 (2001) 687-691. https://doi.org/10.1016/S0921-5093(01)00936-4.

[46] D. Demirskyi, D. Agrawal, A. Ragulya, Comparisons of grain size-density trajectory during microwave and conventional sintering of titanium nitride, J. Alloys. Compd. 581 (2013) 498-501. https://doi.org/10.1016/j.jallcom.2013.07.159.

[47] S. Suarez-Vazquez, M. Nanko, Preparation of dense TiN1− X (X= 0–0.4) by pulsed electric current sintering: Densification and mechanical behavior, Int. J. Refract. Met. Hard. Mater. 44 (2014) 54-59. https://doi.org/10.1016/j.ijrmhm.2014.01.008.

[48] B. M. Moshtaghioun, D. Gómez-García, A. Domínguez-Rodríguez, Spark plasma sintering of titanium nitride in nitrogen: Does it affect the sinterability and the mechanical properties?, J. Eur. Ceram. Soc. 38 (2018) 1190-1196. https://doi.org/10.1016/j.jeurceramsoc.2017.12.029.

[49] D. Stone, K. Yoder, W. Sproul, Hardness and elastic modulus of TiN based on continuous indentation technique and new correlation, J. Vac. Sci. Technol. A. 9 (1991) 2543-2547. https://doi.org/10.1116/1.577270.

[50] H. Sachdev, Influence of impurities on the morphology and Raman spectra of cubic boron nitride, Diam. Relat. Mater. 12 (2003) 1275-1286. https://doi.org/10.1016/S0925-9635(03)00072-4.

[51] M. Dios, Z. Gonzalez, E. Gordo, B. Ferrari, Chemical precipitation of nickel nanoparticles on Ti (C, N) suspensions focused on cermet processing, Int. J. Refract. Met. Hard. Mater. 63 (2017) 2-8. https://doi.org/10.1016/j.ijrmhm.2016.08.009.

[52] A. Leyland, A. Matthews, On the significance of the H/E ratio in wear control: a nanocomposite coating approach to optimised tribological behaviour, Wear. 246 (2000) 1-11. https://doi.org/10.1016/S0043-1648(00)00488-9.

[53] A. Leyland, A. Matthews, Design criteria for wear-resistant nanostructured and glassy-metal coatings, Surf. Coat. Technol. 177 (2004) 317-324. https://doi.org/10.1016/j.surfcoat.2003.09.011.

[54] R. Warren, Measurement of the fracture properties of brittle solids by Hertzian indentation, Acta. Metall. 26 (1978) 1759-1769. https://doi.org/10.1016/0001-6160(78)90087-1.

[55] J.M. Tarragó, J.J. Roa, V. Valle, J. Marshall, L. Llanes, Fracture and fatigue behavior of WC–Co and WC–CoNi cemented carbides, Int. J. Refract. Met. Hard. Mater. 49 (2015) 184-191. https://doi.org/10.1016/j.ijrmhm.2014.07.027.

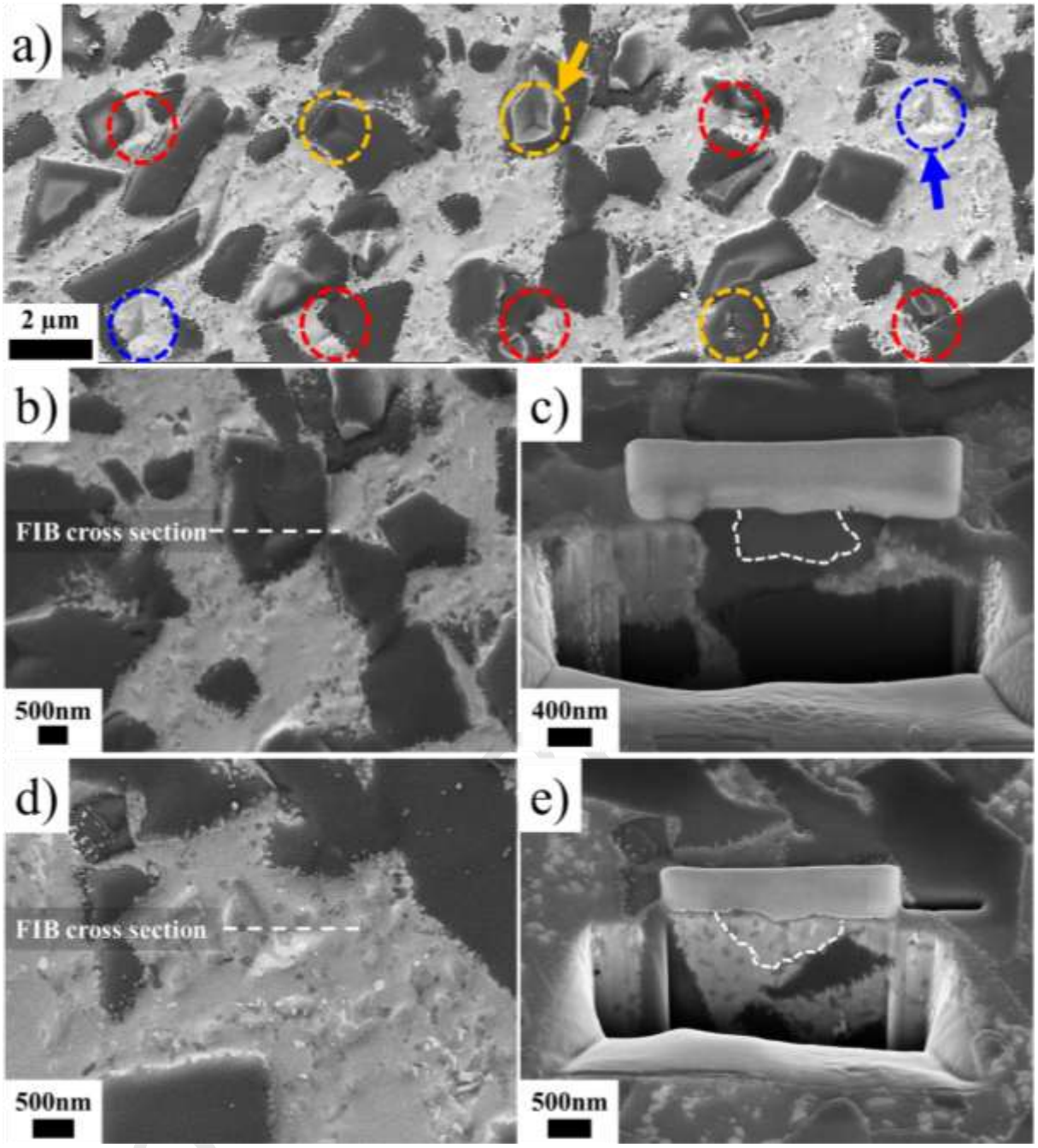

Figure 1. (a) FESEM micrograph of a small array of imprints performed at 200 nm of maximum displacement into surface. (b) and (d) magnified FESEM micrograph of arrowed residual imprints (**Figure 1a**) for cBN particle and TiN binder, respectively; and (c) and (e) FIB-milled cross sections of such imprints, showing estimated size and extension of plastic deformation region induced by nanoindentation.

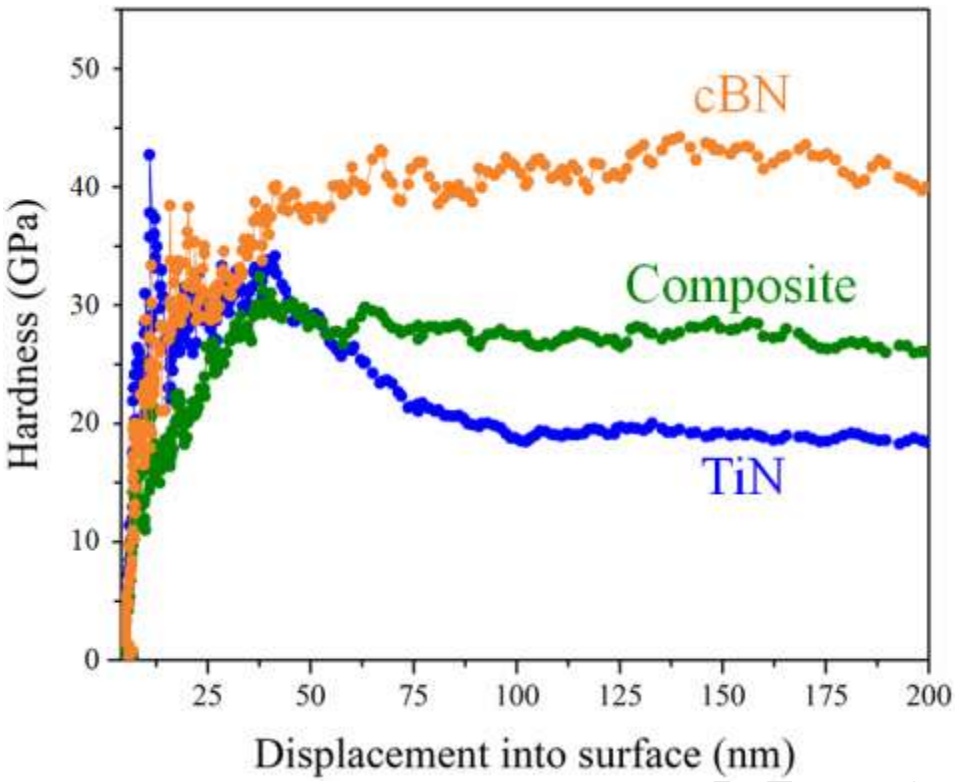

Figure 2. Hardness against displacement into surface for imprints performed at 200 nm of maximum penetration depth and whose residual imprints are probing the three mechanically different phases defined for the PcBN composite studied.

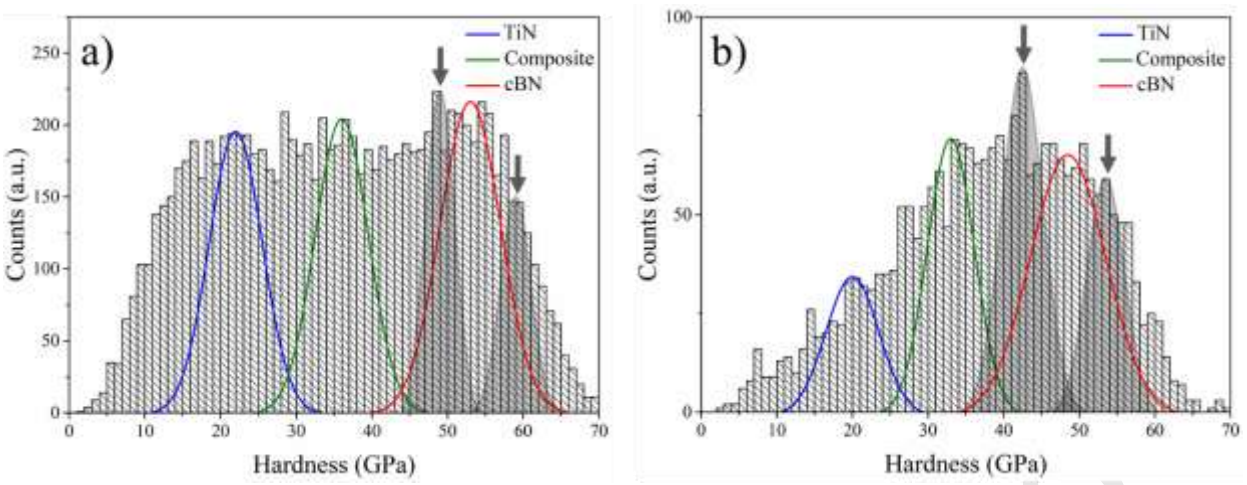

Figure 3. Hardness histograms computed from (a) 12500 indentations performed at 10 mN of maximum applied load, and (b) 2500 indentations performed at 25 mN of maximum applied load.

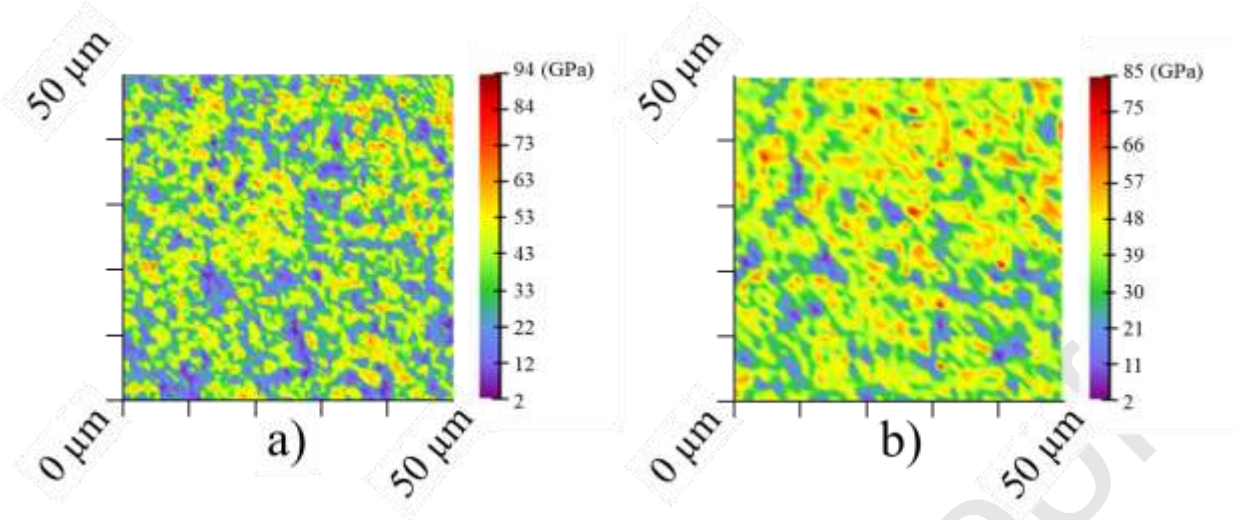

Figure 4. Hardness map evaluated under loading control mode for studied sample with different applied loads. (a) 10 mN and (b) 25 mN.

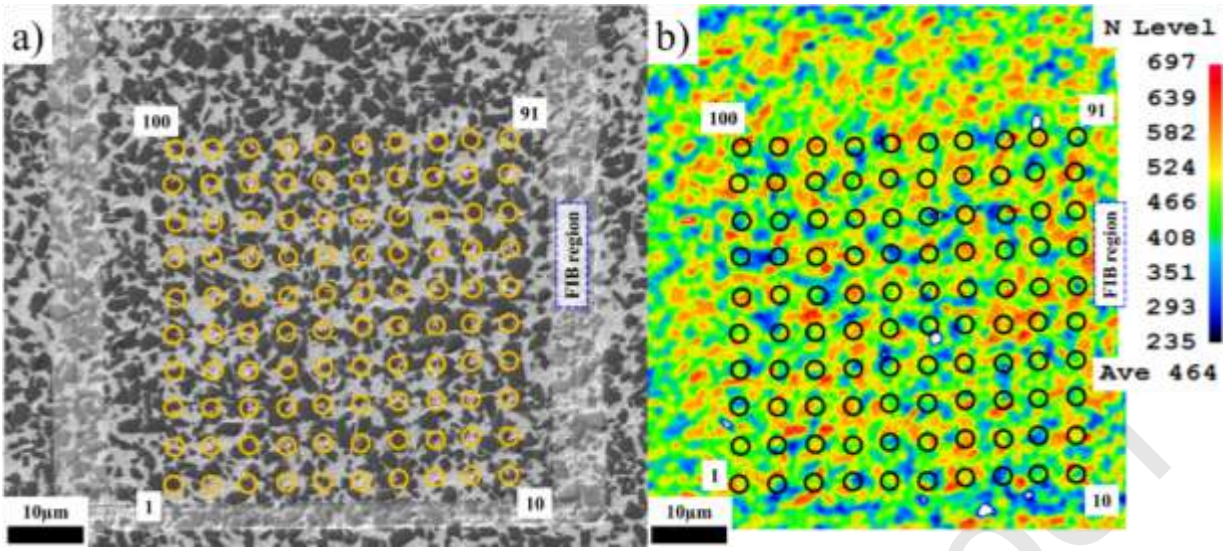

Figure 5. Matrix of indentations (10x10) applied on specific area (framed by a FIB-milled square) of the sample, (a) FESEM micrograph of the region with the matrix of indentations, and (b) N map of corresponding zone with detected by EMPA.

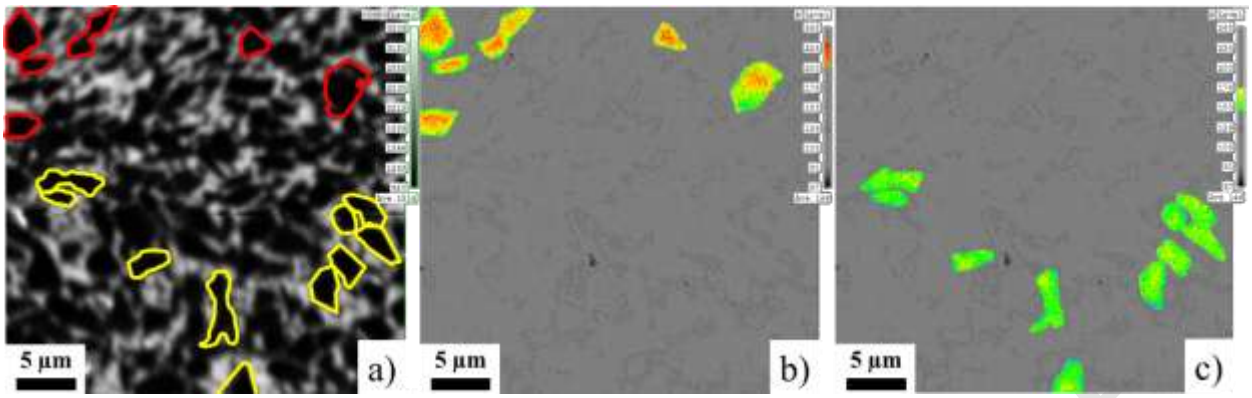

Figure 6. Atomic chemical analysis performed by EMPA: (a) SEM micrograph, (b) N map for High N grains marked by red dashed lines in SEM image, and (c) N map for Low N grains marked by yellow dashed line in the SEM image, which implies low and high B content, respectively.

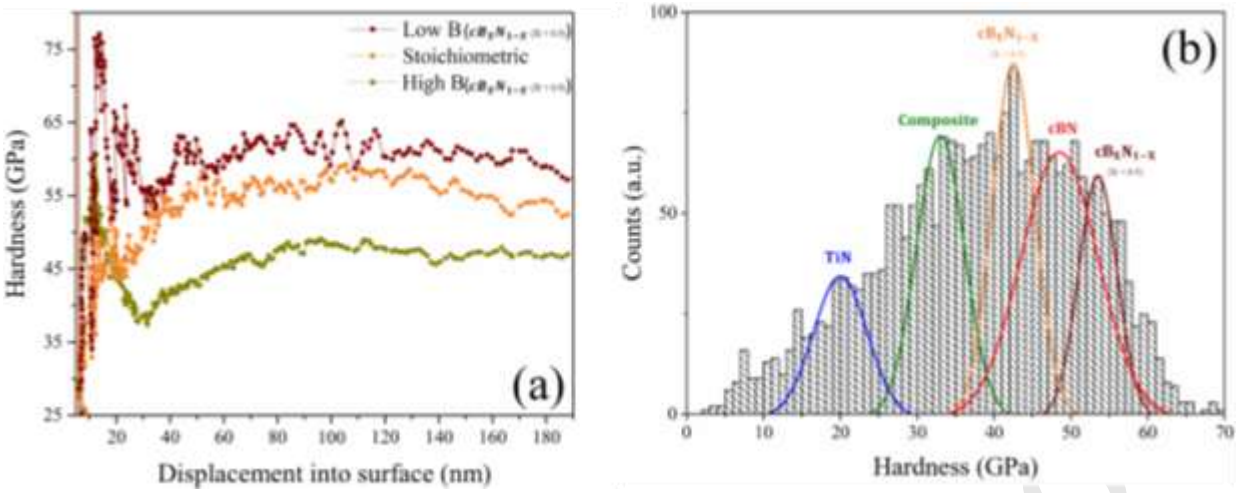

Figure 7. (a) Hardness against penetration depth for cBN particles exhibiting different B (and N) content, assessed from indentations performed in the region observed by EMPA and within individual cBN particles. (b) Hardness histogram determined from 2500 indentations performed at 25mN. Five mechanically different phases were deconvoluted: TiN binder, composite and stoichiometric as well as non-stoichiometric (B-rich and B-poor) cBN particles are overlapped on the histogram.

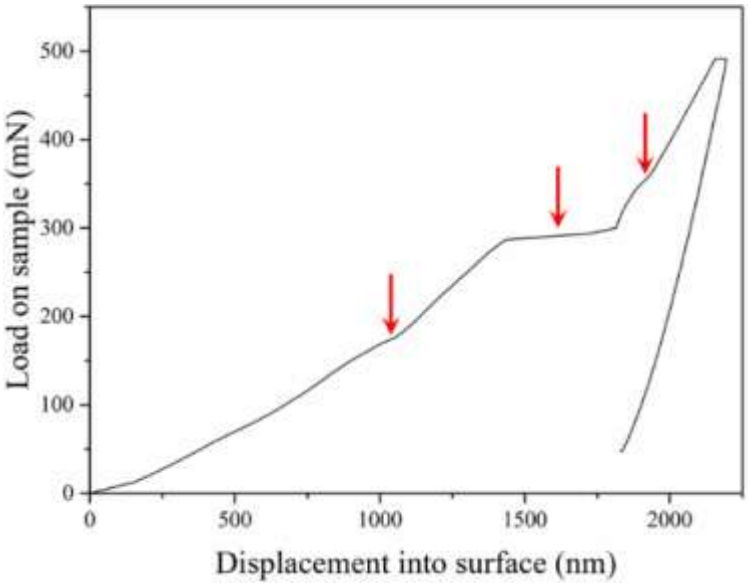

Figure 8. *P* – *h* curve for the indentation performed at 50 gf (red arrows indicate the pop-ins).

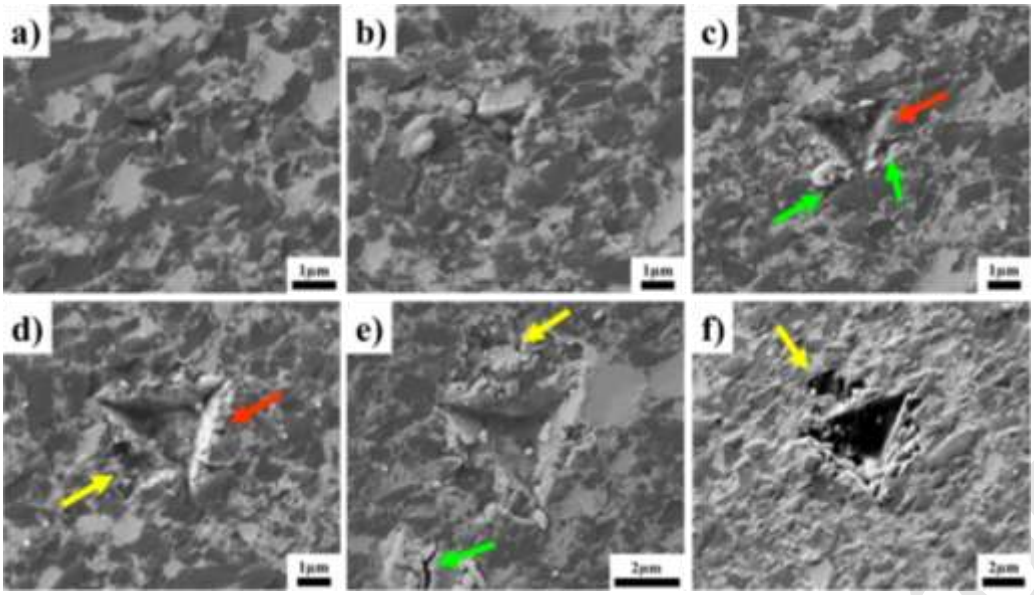

Figure 9. FESEM micrograph of the residual imprint for cube-corner indentations performed at: a) 5, b) 10, c) 20, d) 30, e) 40 and f) 50 gf (Red, green and yellow arrows indicate pile-up, cracks and chipping, respectively).

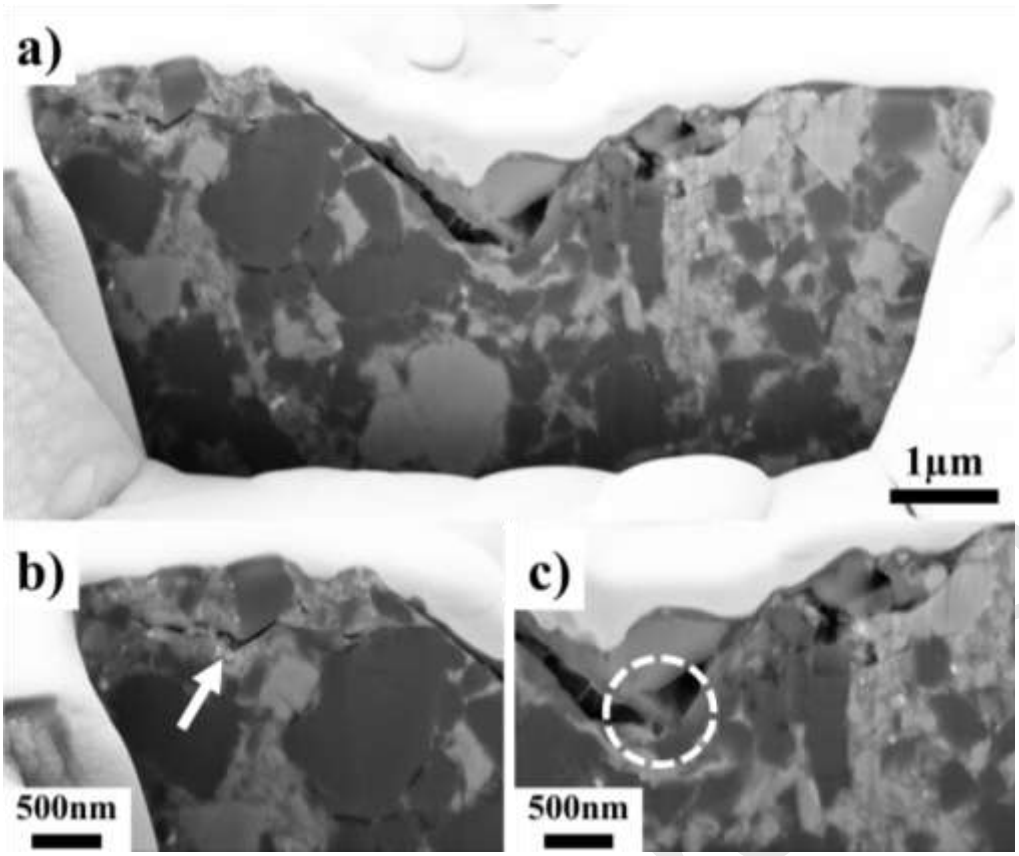

Figure 10. FESEM micrograph of a) the transversal section of the residual imprint performed at 50 gf, b) magnified micrograph indicating lateral cracks with white arrow and c) crack bridging shown with white dashed circle.

Table 1. Chemical composition of constitutive phases for the composite investigated.

Position	Phase	B	N	Al	Ti
1	cBN	46.8	48.8	1.33	3.04
2	TiN	-	25.3	-	74.7

Table 2. Microstructural parameters of PcBN composite studied.

cBN particle size (μm)	TiN binder mean free path, λ (μm)	Vol. % binder
2.7 ± 0.2	2.0 ± 0.1	30

Table 3. Hardness values for each mechanical phase, obtained from the fitting of the experimental values by using statistical analysis.

Phase	Hardness (GPa) (10 mN applied load)	Hardness (GPa) (25 mN applied load)
TiN	23 ± 5	21 ± 5
Composite	36 ± 5	33 ± 5
cBN	53 ± 5	49 ± 7

Table 4. Small-scale *H* for five mechanically different phases of studied sample.

Phase	TiN	Composite	Low N cBN	Stoichiometric cBN	High N cBN
Hardness, H (GPa)	21 ± 5	33 ± 5	43 ± 3	49 ± 7	54 ± 3